



Joint interpretation of magnetotelluric, seismic and well-log data in Hontomín (Spain)

X. Ogaya¹, J. Alcalde², I. Marzan³, J. Ledo⁴, P. Queral⁴, A. Marcuello⁴, D. Martí³, E. Saura³, R. Carbonell³, B. Benjumea⁵

¹Dublin Institute for Advanced Studies, School of Cosmic Physics, Dublin 2, Ireland

²Department of Geology and Petroleum Geology, University of Aberdeen, Aberdeen, United Kingdom

³Institute of Earth Sciences Jaume Almera ICTJA-CSIC, Barcelona, Spain

⁴GEOMODELS Research Institute, Departament de Geodinàmica i Geofísica, Facultat de Geologia, Universitat de Barcelona, Barcelona, Spain

⁵Institut Cartogràfic i Geològic de Catalunya ICGC, Barcelona, Spain

Correspondence to: X. Ogaya (xogaya@cp.dias.ie)

Abstract. Hontomín (N of Spain) hosts the first Spanish CO₂ storage pilot plant. The subsurface characterisation of the site included the acquisition of a 3D seismic reflection and a circumscribed 3D magnetotelluric (MT) survey. This paper addresses the combination of the seismic and MT results, together with the available well-log data, in order to achieve a better characterisation of the Hontomín subsurface. We compare the structural model obtained from the interpretation of the seismic data with the geoelectrical model resulting from the MT data. The models correlate well in the surroundings of the CO₂ injection area with the major structural observed related to the presence of faults. The combination of the two methods allowed a more detailed characterisation of the faults, defining their structural and fluid flow characteristics, which is key for the risk assessment of the storage site. Moreover, we use the well-log data of the existing wells to derive resistivity-velocity relationships for the subsurface formations and compute a 3D velocity model of the site using the 3D resistivity model as a reference. The derived velocity model is compared to both the predicted and logged velocity in the injection and monitoring wells, for an overall assessment of the resistivity-velocity relationships computed. Finally, the derived velocity model is compared in the near surface with the velocity model used for the static corrections in the seismic data. The results allowed extracting information about the characteristics of the shallow subsurface, enhancing the presence of clays and water content variations. The good correlation of the velocity models and well-log data demonstrate the potential of the two methods for characterising the subsurface, in terms of its physical properties (velocity, resistivity) and structural/reservoir characteristics. This work explores the compatibility of the seismic and magnetotelluric methods across scales highlighting the importance of joint interpretation in reservoir characterisation.

1 Introduction

Geophysical characterisation is the main tool to unravel the complex physical properties of the subsurface and is the central part of the characterisation of geological reservoirs. The characterisation of reservoirs dedicated to CO₂ geological storage



requires an extensive preliminary geophysical study according to best practice manuals and reports (e.g., IPCC, 2005; Chadwick et al., 2008), and governmental directives (e.g., EU Directive, 2009). Reflection seismics is a powerful geophysical tool for subsurface imaging and it is largely used to characterise the subsurface for resource exploration (e.g., Hart, 1999; Hesthammer et al., 2001). The interpretation of the seismic images provides important constraints on the geological structures, and the analysis of the data allows inferring information on the subsurface velocity field. However, seismic data is unable to provide information on pore fluids and is not very sensitive to fluid saturation (e.g., Eid et al., 2015). On the other hand, electromagnetics, and more especially the magnetotelluric method (MT) are particularly suitable for fluid characterisation purposes, thanks to their sensitivity to changes in the electrical conductivity of the pore space directly linked to changes in fluid saturation (Bedrosian, 2007; Nakatsuka et al., 2010; MacGregor, 2012). Joint inversion of magnetotelluric and seismic data is a promising practice to resolve different aspects of the same structure (e.g., Gallardo and Meju, 2003), but its application is computationally expensive and the algorithms used are still under development (Moorkamp et al., 2011). Joint interpretation of seismic and electromagnetic data have proven successful in subsurface characterisation (e.g., Harris and MacGregor, 2006; Juanatey et al., 2013; Solon et al., 2015). Hence, a compelling reservoir characterisation will benefit from the integration of the structural interpretation, provided by the seismic image, with the electrical properties derived from the MT method (e.g., Eberhart-Phillips, 1995; Muñoz et al., 2010).

Hontomín, located in the SW portion of the Basque-Cantabrian basin (N of Spain, Fig. 1), hosts the first pilot site in Spain for CO₂ geological storage in a deep saline aquifer. Successful CO₂ storage sites include a complete characterisation, dedicated to understand the characteristics of the subsurface as well as to ensure the suitability, safety and security of the site (e.g., Chadwick et al., 2004; Förster et al., 2006; White, 2013). The selection of Hontomín as a pilot CO₂ storage site motivated a multidisciplinary characterisation of the area, aimed to unravel the main characteristics of the subsurface structures. This includes geochemical (Elío et al., 2013; Nisi et al., 2013; Permanyer et al., 2013), geophysical (Alcalde et al., 2013a; 2013b; 2014; Ogaya et al., 2013; 2014; Ugalde et al., 2013; Vilamajó et al., 2013; 2015; Rubio et al., 2011; Benjumea et al., 2016) and hydro/geomechanical (Canal et al., 2013; Martínez-Landa et al., 2013) studies. Amongst them, this work aims to integrate the seismic (Alcalde et al., 2013a; 2013b; 2014) and MT (Ogaya et al., 2013; 2014) characterisation results together with the available log data to expand our knowledge of the subsurface of Hontomín.

In this paper, we carry out a joint interpretation of the structural model from seismics and the geoelectrical model from magnetotellurics, from a structural and petrophysical point of view. The logged data of the existing wells are used to derive resistivity-velocity relationships for the different formations of the subsurface and compute velocity models using the geoelectrical model as a reference. The static correction model of the site is presented for first time in this work and is correlated with the derived velocity models in order to better characterise the shallow subsurface. The recently available data of the injection and monitoring wells of the Hontomín site are also used to validate the results.



2 Geophysical setting

2.1 Well-log data

The study area has been explored for hydrocarbon resources and contains four hydrocarbon exploration wells drilled between the late nineteen-sixties and 2007 (H1, H2, H3 and H4, Fig. 1). However, their overall production never exceeded 3000 bbl (Permanyer et al., 2013). In 2012 three shallow hydrogeological wells were drilled in the framework of the CO₂ storage project to carry out groundwater studies (GW1, GW2, and GW3 - Benjumea et al., 2016, Fig. 1). Finally, in 2013, the injection (Hi) and the monitoring (Ha) wells were drilled (Fig. 1) as a part of the CO₂ storage plant. The resistivity logged data of the H4, Hi and Ha wells is presented for the first time in this work.

2.2 Seismic dataset

The seismic characterisation in Hontomín included the acquisition of a 36 km² 3D seismic reflection dataset (Alcalde et al., 2013a). The area studied (Fig. 1) ensured the coverage of all the boreholes as well as the entire target dome structure. The quality of the seismic data was hampered by the geological complexity of the study area, summarised in two main geological aspects: (1) the existence of a velocity inversion near the surface produced a loss of first arrival energy in offsets larger than 400 m, creating a so-called “shadow zone” in that portion of the data. (2) The mixed media (siliciclastic and carbonate) present in the sedimentary succession produced sharp changes in the propagation velocity that resulted in a blurred seismic signature. These factors, together to the generally moderate signal-to-noise ratio (S/N ratio) present in onshore-acquired data, resulted in a severe lack of coherency in the deep reflections (Alcalde et al., 2013b). The acquired 3D seismic dataset was processed up to post-stack time migration (Alcalde et al., 2013b). In spite of the improvement of the resulting image obtained by the processing applied, the limited lateral continuity of the reflections obstructed a direct interpretation of the seismic data. This issue was circumvented by the use of a conceptual model to guide the interpretation (Alcalde et al., 2014). This conceptual model was generated from the available well-log and regional geology data. Further details on the acquisition, processing and interpretation of the 3D seismic dataset are in-depth described in Alcalde et al., (2013a, 2013b and 2014, respectively).

2.2.1 Structural model

The structural model was built from the interpretation of the seismic dataset combined with the available well-logs and regional geology (Alcalde et al., 2014). The well-log data allowed identifying 39 subunits from 12 major units ranging from the Anhydrite Unit at the bottom to the Cenozoic sediments at the top of the wells. The top surfaces of 9 of these 12 major units were interpreted in the seismic volume (Fig. 2.a). Four sets of faults were also interpreted in the seismic data, the “S-”, “E-”, “N-” and “X-faults” (Fig. 2.c). The interpreted surfaces allowed inferring a prognosis for the Hi and Ha wells (Alcalde et al., 2014) which successfully forecasted the depths of the formations in the drilling areas.



The nine main surfaces and the four sets of faults allowed understanding the geometries of the subsurface structures in Hontomín (Fig. 2b). The target dome structure is formed by the Jurassic carbonate sediments and cored by Triassic evaporitic sediments (anhydrite and salt). The target reservoir is a saline aquifer hosted in the Limestone Lias unit and located in the injection area at 1485m depth. It is covered by the main seal formation (Marly Lias) composed by marlstones, marly limestones and interbedded black-shales levels. The dome is overlaid by Lower Cretaceous siliciclastic sediments (Weald, Escucha and Utrillas fm.) which progressively flatten and lose the dome geometry upwards. The top of the sedimentary sequence is composed by Upper Cretaceous limestones and Cenozoic sediments, outcropping in the study area (Fig. 1). The Upper Cretaceous sediments are karstified, but the extent and geometry of the karstic areas is relatively unknown. Two major faults, S-1 and E-1 (hereafter “South Fault” and “East Fault”, respectively) affect the entire stratigraphic sequence (Fig. 2b). They also dominate the structural relief of the Jurassic dome, dividing the area in three blocks (Fig. 2.c): central, eastern and southern blocks. The slip of the faults locate the central block (that includes the target injection area) structurally higher than the eastern and southern blocks.

2.3 Magnetotelluric dataset

The magnetotelluric characterisation of the Hontomín site was divided into two stages: a 2D MT data acquisition carried out in Spring 2010 (Ogaya et al., 2013) and a 3D MT data acquisition undertaken in Autumn 2010 (Ogaya et al., 2014). In total, a grid of 109 closely-spaced broadband magnetotelluric (BBMT) sites was collected covering an areal extent of 3x5 km² (Fig. 1). The BBMT data were mainly organised along five NS profiles of around 4 km long and the average distance between them was approximately 500 m. Two smaller profiles were acquired in the injection area to refine the grid in the target region. The stations were distributed at 200 m intervals along the profiles and the data were acquired in the period range of 0.001 to 100 s. The longer the recorded periods, the deeper is the penetration depth and the lower is the resolution of the magnetotelluric method. The dataset for the 3D inversion contained the full impedance tensor (MT tensor that relates the orthogonal components of the electric and magnetic field variations recorded on the surface) of 102 BBMT sites in the range of 0.001 to 10 s. Seven BBMT sites and periods longer than 10 s were discarded for being too noisy. Further details on the acquisition, processing, inversion and modelling of the MT data are in-depth described in Ogaya et al., (2013 and 2014).

2.3.1 Geoelectrical model

The resistivity baseline model of the Hontomín site reveals a geoelectrical structure composed of four main layers (Fig. 3; Ogaya et al., 2014): a resistive bottom layer R1 (below -600 m.a.s.l.) linked to Keuper facies and to an Anhydrite unit; a conductive layer C1 (below -200 m.a.s.l. and thickness up to 400 m) containing the primary reservoir and seal units; a resistive middle layer R2 (between +700 m.a.s.l. and -200 m.a.s.l.) containing the secondary reservoir-seal system, and a conductive top layer C2 (above +700 m.a.s.l.) linked to Upper Cretaceous and Cenozoic materials.

The model shows a smooth dome-like geoelectrical structure with an approximate NW-SE orientation (Fig. 3; Ogaya et al., 2014). The crests of the four interpreted layers move along this direction, from the SE corner (R1) to the NW corner (R2) of



the study area. The injection area is located approximately in the crest of the C1 layer, which have an extension of circa 1x1 km² (Fig. 3g). The saline aquifer (main reservoir) is linked to the most conductive region inside the C1 layer (Fig. 3g). The slope of the north flank is less steep and seems to be elongated to the NW. The R2 layer begins at circa 180 m.a.s.l. and its base is located to the SE of the study area, in the location of the injection and exploration wells (Fig. 3d). Upwards, this layer progressively migrates to the NW, until reaching approximately 664 m.a.s.l. at its top. In the southern part of the model, a fault region (“F region”) was imaged. The EW dashed line in Fig. 3 indicates the approximate north-border of that region. The geoelectrical structure of the F region revealed an important conductive fluid circulation along the fault zone, which was unknown until the MT survey was conducted. The F region is observed to be more conductive in the eastern part than in the western part, where it seems to unfold in different faults (Fig. 16 in Ogaya et al., 2014). The model suggested that the F region affects all the layers of the model but it does not outcrop at surface (Ogaya et al., 2013; 2014). In general, the R2 layer is more resistive in the eastern part of the model (Fig. 3c,d,e). This could be due to the presence of the East fault (Fig. 2) which affects the geoelectrical structure of the eastern part of the model area despite being located outside the area covered by the MT survey (Ogaya et al., 2014). Small resistivity variations are observed inside the R2 layer (“FR2” areas) that could be associated with a set of minor faults in the Dogger and Purbeck units (Ogaya et al., 2014).

The drilling of the Hi and Ha wells was completed at the end of 2013 and their resistivity log data only became available after the publication of the 3D MT model (Ogaya et al., 2014). The agreement between the geoelectrical structure predicted by the 3D resistivity model for the Hi and the Ha wells and their resistivity log data confirms the accuracy and reliability of the geoelectrical model (Fig. 4). The 1D resistivity models displayed in red correspond to the column of the 3D geoelectrical model located at each well position. The 1D models are very similar to each other because they belong to adjacent cells of the 3D mesh (the distance between the Hi and Ha wells is 50 m).

3 Joint interpretation: Seismic structural model – resistivity model

Two sections of the structural model, profiles α and β presented in Alcalde et al., 2014, have been compared to their equivalents in the geoelectrical model, profiles I and III presented in Ogaya et al., 2014 (Fig. 5). These two sections cross different wells in the area (see Fig. 1): profile I crosses wells H4, H2, H1, GW2 and GW1, and profile III, wells H3 and H2.

There is a general agreement between the top of the different units displayed in the structural model interpreted from the seismics, and the top of the bodies imaged in the geoelectrical model in the centre of the study area. The match is not perfect in the flanks of the dome, where the steepness of the flanks imaged by the seismic data is higher than that observed in the MT image. This mismatch is probably partially related to the presence of the South fault (Fig. 5). The plane of the South fault in the structural model coincides with the bend of the resistive body R2 and with the position of the F region interpreted in the geoelectrical model. The geoelectrical characteristics suggest that the fracture zone related to the South fault is a region of ongoing fluid flow. The South fault is also interpreted in the structural model as a flower structure with multiple splays, and this correlates well with the apparent multiple branching observed in the western part of the conductive F region



of the resistivity model (Fig. 16 in Ogaya et al., 2014). In the eastern part of the model (Fig. 5b), the South fault coincides with the region where the R2 body is more resistive. The East fault interpreted in the structural model (plotted in orange in Fig. 5 and called EF in the geoelectrical models) is out of the MT survey region modelled by the MT method but the joint interpretation of the two models seems to certify that it is responsible of the more resistive behaviour of the R2 layer on that part of the model. We have associated the resistive characteristics of this area to a potential sealing of the East fault. The slight changes observed in the R2 resistivity layer could be associated to the presence of the N faults (in white in Fig. 5). However, since the resistivity changes observed in the geoelectrical model are not obvious, we cannot anticipate fluid circulation along these fractures. The X faults (in yellow in Fig. 5) were not imaged in the geoelectrical model, being their size below the resolution of the MT method at that depth. The minor faults FR2 detected in the geoelectrical model (Fig. 5) are not observed in the structural model. This could be due to the existence of small scale faults or fractures, with small displacement but sufficient fluid circulation to produce resistivity changes in the R2 layer.

4 Deriving velocity from resistivity

4.1 Resistivity-velocity relationships

Resistivity-velocity relationships have been used to calculate one physical parameter as a function of the other in many works (e.g. Faust, 1953; Brito dos Santos et al., 1988; Hacikoylu et al., 2006; Werthmüller et al., 2013). In Hontomín, the log data of the GW1 and the H4 wells were used to derive resistivity-velocity relationships for all the formations and compute a 3D velocity model of the site, using the 3D resistivity model as a reference. These two wells were chosen because of their suitable location in the surroundings of the injection area (Fig. 1) and the availability of their almost complete resistivity and velocity log data. The GW1 data were used for the shallow subsurface, from 24.35 m to 400 m depth, and the H4 data for the deeper structures, from 456 m depth to the end of the borehole at 1611 m.

The resistivity (R)-velocity (V) log pairs were grouped based on their depth and their relative behaviour (i.e., direct or inverse relationship). In this way, the GW1 log data were divided into five groups (S-groups) and the H4 log data into twelve groups (D-groups). Two empirical relationships were calculated for each group: (i) a linear regression of V vs log(R) to test a simple relationship between the two properties (ER1 hereafter, Table 1, Fig. 6a,c) and (ii) a linear regression of R/V vs R to reproduce the data more accurately (ER2 hereafter, Table 2, Fig. 6b,d).

Thereby, the empirical relationship ER1 is of the type

$$V = a \log R + b, \quad (1)$$

where a and b are constants determined by regression analysis for each group (Fig. 6a,c). Table 1 details the value of the constants and the accuracy of the fit. On the other hand, the empirical relationship ER2 is of the type

$$V = \frac{R}{cR + d}, \quad (1)$$



where c and d are also constants determined by regression analysis for each group (Fig. 6b,d). Table 2 details the value of the constants and the accuracy of the fit. In general, relationships ER1 and ER2 have similar behaviour although they present two important discrepancies: relationship ER1 provides negative velocity values for resistivities below 5 Ωm , and relationship ER2 is less sensitive to variations for resistivity values approximately higher than 900 Ωm .

5 4.2 Validation of the relationships

The 3D resistivity model (model R from now on) was converted into two different velocity models using the above mentioned resistivity-velocity relationships: model “ V_{R1} ” for relationship ER1 and model “ V_{R2} ” for relationship ER2. The accuracy of these conversion relationships was assessed comparing the velocity log data of the GW1 and the H4 wells (in black in Fig. 7) with the 1D velocity model provided by V_{R1} (in green in Fig.7) and V_{R2} (in red in Fig. 7) for each well.

10 These 1D models are the velocity values of the column of the 3D model located at the position of each well. They reproduce the velocity pattern of both wells and hence there is good match between the log data and the obtained velocity models. For the shallow subsurface, relationship ER2 seems to provide an overall slower velocity model than ER1 at the GW1 well location (Fig. 7a). For deeper part, relationship ER2 seems to be in general faster than ER1 at the H4 well position (Fig. 7b). We observe a quite narrow low velocity zone at 1200 m depth that is imaged in none of the velocity models, neither V_{R1} nor

15 V_{R2} (Fig. 7b). This is reasonable, since the V_R models were computed using magnetotellurics and the thickness of this layer is below the resolution of the method at that depth.

Alcalde et al. (2014) calculated the average petrophysical properties for all the formations using the well-log data of all the existing wells. We used the average velocities (called “ V_{AVG} ” hereafter) to compute the equivalent 1D velocity models for the GW1 and the H4 wells (in blue in Fig. 7). The difference between the V_R models and V_{AVG} gives an idea of the error of

20 our velocity models in all the study area (Fig. 7c). For depths shallower than 200 m, area where the log data of the GW1 well are noisier, the differences between the models are big (bigger than 2000 m/s). However, for depths ranging between 200 and 400 m the log data are less noisy and the discrepancies between the models are below 250 m/s. For depths deeper than 400 m (H4), there is also a good agreement between the models. The highest discrepancies (above 1000 m/s) correspond to layers with a thickness below the resolution of the MT method.

25 We also compared the velocity models provided by the V_{R1} and V_{R2} models for the Hi and Ha wells with the prognosis of these two wells published in Alcalde et al. (2014) (V_{AVG}) as well as with the later acquired velocity logs. Figure 8 shows that in general, the differences between the three models are similar to the ones observe for the GW1 and the H4 well (Fig. 8). However, the agreement between the models in the shallowest part (first 200 m) of the Hi well is considerably better than in the Ha well. For the deeper section, the main differences are located at depths of 500 m, 1000-1200 m and 1500 m

30 approximately.

The available velocity log data ranges from 10 m to 200 m for the Hi well and from 600 m to 1284 m for the Ha well. The first 200 m of the Hi well-log are well reproduced by all the models (Fig. 8). For depths ranging between 1000 m and 1200 m, the prognosis reproduces better the velocity behaviour than the V_{R1} and V_{R2} models. This is reasonable since, as was also



seen in Fig. 4, the resistivity model does not image the more resistive layer located at that depth successfully. At 1500 m depth we do not have velocity log data but one would expect a behaviour similar to the one observed in the H4 well at that depth. Thus, we associate the differences between the V_R models and the prognosis to the lower resolution of the MT method at that depth.

5. Shallow subsurface

5.1 Static correction model

Near surface sediments (e.g., weathering layer, loose sediments or volcanic stockworks) often produce velocity variations that can affect the arrival time of the energy to the recording geophones, especially in onshore data (Taner et al., 1998; Tryggvason et al., 2009). These areas are usually heterogeneously distributed and commonly feature low propagation velocities. This causes unwanted delays in the traces and subsequent disturbances in the coherency of deeper reflections (Juhlin, 1995). Refraction static corrections are standardly used to mitigate this problem (e.g., Malehmir and Bellefleur, 2009). This method uses the differences in travel-time of the first-breaks to calculate the replacement velocity of a near-surface layer, based on traveltimes inversion (Lawton, 1989). This velocity model is then used to calculate the time-shifts in the needed to minimise the travel-time difference, usually enhancing considerably the coherence of the reflections.

Refraction statics proved to be the processing step that improved the most the quality of the Hontomín seismic data, in spite of the loss of first arrivals at offsets larger than circa 400 m (Alcalde et al., 2013b). Due to this “shadow zone”, the first arrival picking was performed manually in more than 670.000 traces, at offsets ranging from 0 to 500 m. The refraction statics corrections were calculated using a seismic velocity model computed by least squares fitting (Woodward, 1991). The resulting velocity model (Fig. 9) represents a replacement velocity of the first 40 m of sediments. It provided static corrections of 0 to 40 ms (RMS of circa 8 ms), with residual statics below 4 ms.

The high density of first-break pickings used (over 18.000 per km²) ensured a robust calculation of the replacement velocity. The statics velocity model (Fig. 9) shows a great amount of detail and a remarkably good correlation with the surface geological map (Fig. 1). The initial model used in the static calculations was a simple half-space model with a constant velocity of 2900 m/s, not containing *a priori* geological information. Hence, this good congruence between the outcrop geology and the statics model ensures the reliability of the statics calculations.

The statics model shows a distinct contrast between higher velocities (over 3000 m/s) in the Central block and areas with lower velocities (below 2750 m/s) in the South and East blocks (Fig. 9). This zoning clearly corresponds to the Upper Cretaceous (higher velocity) limestones and the Cenozoic (lower velocity) fluvial sediments, which outcrop in the study area (Fig. 1). These two areas are divided by two high velocity lineated features, oriented approximately E-W and N-S. These lineations correlate remarkably well with the locations of the East and South faults. The East fault does not outcrop in the study area and the presence of the South fault at the surface is unclear. However, their influence in the Hontomín structure is clear, as only 40 m below the surface they mark the boundary between high and low velocity sediments. The small-scale low



velocity areas scattered across the Upper Cretaceous sediments could have their origin in the intense karstification observed in these otherwise high-velocity limestones (Quintà and Tavani, 2012). A high velocity zone located in the eastern margin of the survey area (Fig. 9) corresponds to an area with very low acquisition fold (Alcalde et al., 2013a), and thus has been discarded from the interpretation.

5 5.2 Joint interpretation: Static correction model – Resistivity-derived models

The static correction model displays the replacement velocities for the first 40 m (Fig. 9). In order to correlate the structures imaged in this model with the ones displayed in the geoelectrical model (model R), we computed a resistance model (i.e., the inverse of the conductivity-thickness product) for the shallow subsurface (Fig. 10a). This was calculated using the resistivity values provided by the R model for depths up to 40 m (following the topography of the model). The resistance model (Fig. 10b) shows resistance values ranging between 0.5 and 6 Ω approximately. The BBMT data acquired in the area surrounding the windmills are noisier than the rest (see Fig. 7 in Ogaya et al., 2014) and it is characterised in the model R by lower resistivity values. The high noise recorded means that the resistivity model R and all the models generated from it have also lower quality in that region. The resultant resistance model (Fig. 10b) shows certain similarities with the static model (Fig. 10a), in which high resistance values (in red) can be correlated with high velocity areas (in red) and vice versa. The resistance model shows a higher nucleation, i.e. a greater amount of scattered bodies than the static model.

In order to evaluate the compatibility of the two methods to image the shallow subsurface, we computed the replacement velocities for the first 40 m of the velocity models V_{R1} (computed using relationship ER1, Fig. 10c) and V_{R2} (computed using relationship ER2, Fig. 10d). In both cases, the topography of the area was taken into account. The two models display similar slower (in blue) and faster (in red) regions but the relationship ER1 (Fig. 10c) provides a smoother result and shows a gentle range of velocity variations. On the other hand, relationship ER2 (Fig. 10d) reproduces better the heterogeneities observed in the resistance model (Fig. 10b) and the velocity values seem to be more extreme (in general, higher and lower velocity values). Both models show that the South fault marks the northern limit of a slower velocity area.

Since the two velocity models display the same velocity structure and the bodies are better defined in the model derived using relationship ER1, we used the V_{R1} model (Fig. 10c) in the comparison with the static correction model (Fig. 10a). In general, the two models reveal similar velocity patterns, with the South fault marking the limit between higher velocities to the North and lower velocities to the South. The area surrounding the windmills shows a remarkably velocity variation between the models. This area corresponds to the noisiest area in the resistivity model R, and hence, this area is discarded for a further interpretation. The South block (located to the south of the South fault) is characterised by slow velocities in both models, but has more structures in the model derived from the resistivity model. The sediments in this area are mainly composed by Quaternary sandstones (gravel and clay) and Cenozoic sandstones (sandstones and clay)(Fig. 1). The different clay content of that area could explain the velocity variations observed in the model derived from the resistivity model (Fig. 10c): the magnetotelluric method is especially sensitive to areas of low resistivity, which would convert into low velocity areas in the derived velocity models. In this case, the areas with higher clay content (in yellow in Fig. 1) would be



represented by low-resistivity values and would produce low velocities. The accumulation of gravel and sandstones in the South block could also imply different levels of water content which could result in important resistivity variations. Finally, the high velocity area displayed to the north to the South Fault show the highest velocity values in the two models, but has more lateral continuity in the static correction model. The most significant difference is observed in the southwestern part of that high velocity area: it corresponds to a homogeneous area in the static correction model whereas has a ring shape with a low velocity area in the middle, in the model derived from the resistivity model (SW part of the Central block in Fig. 10c). The accumulation of clays could also be responsible for the low velocity areas observed in the centre of this ring. The minor discrepancies between the two models observed in this Central block could be originated by the existence of karstic structures.

10 5 Discussion

The joint interpretation of the seismic and magnetotelluric data acquired at the Hontomín site is analysed from a structural and a petrophysical point of view. Firstly, it is difficult to establish a direct structural link between the two datasets because of the nature of the two methods (i.e., the resistivity model does not image lithologies but geoelectrical properties). However, the depth and geometry of the main resistive layers agree with the structure defined by the different surfaces in the centre of the study area (i.e. the area covered by the boreholes). Outside this area, the presence of the South and the East faults alter the geoelectrical behaviour of the different layers and produces the major differences observed between the models. The correlation of the two models provides a twofold characterisation of the existing faults, contributing to a greater structural constrain and allowing to estimate the important hydrogeological properties. For instance, the South fault seems not to have an important displacement in the structural model but could be associated to an important fluid circulation according to the resistivity model, especially in the eastern part. In the same way, some minor resistivity changes imaged in the Dogger and Purbeck facies could suggest a small fluid circulation along small fractures that are not observed in the seismic data, potentially due to very small or inexistent vertical displacement. Understanding these hydrogeological properties is essential for ensuring the safety of the CO₂ site and to forecast the behaviour of the injected CO₂ in the case of unforeseen leakage events.

From a petrophysical point of view, we derived a velocity model from the resistivity (MT) model using the available log data. Despite the level of resolution of the MT method is different than in the other two techniques (i.e., well-log data and seismics), it has proven its capability to provide satisfactory velocity models of the site. The quality of the derived velocity models is expected to be higher in the centre of the study area (in the surroundings of the wells) than in those areas where the existence of the South and the East faults strongly alter the geoelectrical behaviour of the different layers.

In the shallow subsurface, the comparison between the static correction model and the derived velocity models for the first 40 m showed relatively small discrepancies between the two models. These discrepancies are reasonable since, apart from the error inherent to the approach, one model was computed from seismic (i.e., sensitive to velocity/density changes) and the



other was computed from magnetotelluric (i.e., sensitive to electrical conductivity) data. Hence, the correlation of the two methods gives a more complete information of the shallow sediments, enhancing the presence of clays and possible variations in water content. On the other hand, the joint interpretation of the two models provides little information about the extent and geometry of the existing karstic areas. The 3D seismic and 3D MT surveys were designed for imaging deeper structures, including the target reservoir and seal formations which are located circa 1.5 km deeper. Thus, capturing the inherent complexity of the karst (i.e., variable size, composition of the filling of the voids, seasonal variation of the water table, potential cementation) could be out of the limits of resolution of the methods applied in this work. An interesting task to face in the future would be to merge these results with other geophysical (e.g., Benjumea et al., 2016) and geochemical (Elio et al., 2013; Nisi et al., 2013) studies carried out in the area, to better constrain the location and geometry of the karst.

In reference to the resistivity-velocity relationships, we derived two different relationships to convert the resistivity model to a velocity model: (i) a linear regression of V vs $\log(R)$ –ER1- and (ii) a linear regression of R/V vs R –ER2-. Based on the obtained results, the used of more than one empirical relationship is advisable because the discrepancies between the different velocity models indicate areas with higher and lower agreement, helping to constrain the error and the accuracy of the approaches. Despite relationship ER2 seemed to reproduce much better than ER1 the pattern of the log data, the derived velocity models are very similar.

The joint interpretation presented here contributes to the better understanding of the Hontomín site subsurface. Both the prognosis presented in Alcalde et al. (2014) and the resistivity model presented in Ogaya et al. (2014) predicted the structure and the physical properties of the recently drilled Hi and Ha wells accurately. Facing the future, the work presented here constitutes a valuable starting point for a joint inversion of the seismic and magnetotelluric datasets. This could provide a more constrained understanding of the fluid circulation along the faults, which have important implications for the safety of the CO₂ storage pilot site.

6 Conclusions

The joint interpretation of the structural, velocity and resistivity model contributes to a more robust understanding of the subsurface, better characterising the existing faults -key aspect for the risk assessment of the Hontomín pilot storage site. The combined interpretation of the geoelectrical and the structural model derived from the seismic data allowed estimating the fluid flow characteristics of the major faults in the area. The methodology used to derive velocity from resistivity has been successfully applied at the Hontomín site, pointing out the importance of employing more than one empirical relationship between the properties to have a better control of the uncertainties inherent to the approach. The joint interpretation for depths shallower than 40 m allowed extracting information about the characteristics of the shallow sediments, highlighting variations in clay and water content. The seismic and magnetotelluric methods have shown their compatibility across scales, pointing out the importance of joint interpretation in characterisation surveys. This work provides a more complete picture of



the Hontomín site subsurface, essential in the monitoring of the site, and establishes the basis for a potential joint inversion of the two geophysical datasets.

Acknowledgements

This work is dedicated to the memory of Andrés Pérez-Estaún, brilliant scientist, colleague and friend. Xènia Ogaya is currently supported in Dublin Institute for Advanced Studies by a Science Foundation Ireland grant IRECCSEM (SFI grant 12/IP/1313). Juan Alcalde is currently funded by the UK Natural Environment Research Council (NERC) – grant NE/M007251/1. Juanjo Ledo, Pilar Queralt and Alex Marcuello thank Ministerio de Economía y Competitividad grant CGL2014-54118-C2-1. Funding for this Project has been partially provided by the Spanish Ministry of Industry, Tourism and Trade, through the CIUDEN-CSIC-Inst. Jaume Almera agreement (ALM-09-027: Characterization, Development and Validation of Seismic Techniques applied to CO₂ Geological Storage Sites) and CIUDEN-Fundació Bosch i Gimpera agreement (ALM-09-009 Development and Adaptation of Electromagnetic techniques: Characterisation of Storage Sites). The CIUDEN project is co-financed by the European Union. The CIUDEN project is co-financed by the European Union through the Technological Development Plant of Compostilla OXYCFB300 Project (European Energy Programme for Recovery).

References

- Alcalde, J., Marzán, I., Saura, E., Martí, D., Ayarza, P., Juhlin, C., Pérez-Estaún, A., and Carbonell, R.: 3D geological characterization of the Hontomín CO₂ storage site, Spain: Multidisciplinary approach from seismic, well-log and regional data, *Tectonophysics*, 2014.
- Alcalde, J., Martí, D., Calahorrano, A., Marzán, I., Ayarza, P., Carbonell, R., and Juhlin, C. and Pérez-Estaún, A.: Active seismic characterization experiments of the Hontomín research facility for geological storage of CO₂, Spain, *International Journal of Greenhouse Gas Control*, 19, pp.785–795, 2013a.
- Alcalde, J., Martí, D., Juhlin, C., Malehmir, A., Sopher, D., Saura, E., Marzán, I., Ayarza, P., Calahorrano, A., Pérez-Estaún, A., and Carbonell, R.: 3-D reflection seismic imaging of the hontomín structure in the basque-cantabrian Basin (Spain), *Solid Earth*, 4(2), 481–496, 2013b.
- Bedrosian, P.A.: MT+, Integrating Magnetotellurics to determine Earth Structure, Physical State and, Processes, *Surveys in Geophysics*, 28, 121-167, doi: 10.1007/s10712-007-9019-6, 2007.
- Benjumea, B., Macau, A., Gabàs, A., and Figueres, S.: Characterization of a complex near-subsurfaces structure using well logs and passive seismic measurements, *Solid Earth*, Submitted, 2016.
- Brito dos Santos, W. L., Ulrych, T. J., and De Lima, O. A. L.: A new approach for deriving pseudovelocity logs from resistivity logs, *Geophysical Prospecting*, 36, 83-91, 1988.



- Canal, J., Delgado, J., Falcón, I., Yang, Q., Juncosa, R., and Barrientos, V.: Injection of CO₂-saturated water through a siliceous sandstone plug from the Hontomín test site (Spain): Experiment and modelling, *Environmental Science and Technology*, 47 (1), 159-167, 2013.
- Chadwick, R. ., Zweigel, P., Gregersen, U., Kirby, G. Holloway, S., and Johannessen, P.: Geological reservoir
5 characterization of a CO₂ storage site: The Utsira Sand, Sleipner, northern North Sea, *Energy*, 29(9-10), 1371–1381, 2004.
- Chadwick, A., Arts, R., Bernstone, C., May F., Thibeau, S., and Zweigel, P.: ‘Best practice for the storage of CO₂ in saline aquifers’, *British Geological occasional Publication*, 14, 2008.
- Eberhart-Phillips, D., Stanley, W. D., Rodriguez, B. D., and Lutter, W. J.: Surface seismic and electrical methods to detect fluids related to faulting, *Journal of Geophysical Research*, 100, 12919, 1995.
- 10 Eid, R., Ziolkowski, A., Naylor, M Pickup, G.: Seismic monitoring of CO₂ plume growth, evolution and migration in a heterogeneous reservoir: Role, impact and importance of patchy saturation, *International Journal of Greenhouse Gas Control*, 43, 70–81, 2015.
- Elío, J., Nisi, B., Ortega, M.F., Mazadiego, L.F., Vaselli, O., and Grandia, F.: CO₂ soil flux baseline at the Technological Development Plant for CO₂ Injection at Hontomín (Burgos, Spain), *International Journal of Greenhouse Gas Control*, 18,
15 224-236, 2013.
- European Union (EU): Directive 2009/31/EC of the European Parliament and of the council of 23 April 2009 on the geological storage of carbon dioxide and amending Council Directive 85/337/EEC, European Parliament and Council Directives 2000/60/EC, 2001/80/EC, 2004/35/EC, 2006/12/EC, 2008/1/EC and Regulation (EC) No 1013/2006, 2009.
- Faust, L. Y.: A velocity function including lithologic variation, *Geophysics*, 18, 271–288, 1953.
- 20 Förster, A., Norden, B., Zinck-Jørgensen, K., Frykman, P., Kulenkampss, J., Spangerberg, E., Erzinger, J., Zimmer, M., Kopp, J., Borm, G., Julin, C., Cosma, C., and Hurter, S.: Baseline characterization of the CO₂SINK geological storage site at Ketzin, Germany, *Environmental Geosciences*, 13(3), 145-161, 2006.
- Gallardo, L. A., and Meju, M. A.: Characterization of heterogeneous near-surface materials by joint 2D inversion of DC resistivity and seismic data, *Geophysical Research Letters*, 30(13), 1658, doi: 10.1029/2003GL017370, 2003.
- 25 Hacikoylu, P., Dvorkin, J., and Mavko, G.: Resistivity-velocity transforms revisited, *The Leading Edge*, 25(8), 1006-1009, doi: 10.1190/1.2335159, 2006.
- Harris, P., and MacGregor, L.: Determination of reservoir properties from the integration of CSEM and seismic data, *First Break*, 24, 15-21, 2006.
- Hart, B. S.: Definition of subsurface stratigraphy, structure and rock properties from 3-D seismic data, *Earth-Science
30 Reviews*, Volume 47, Issues 3–4, Pages 189-218, 1999.
- Hesthammer, J., Landrø, M., and Fossen, H.: Use and abuse of seismic data in reservoir characterisation, *Marine and Petroleum Geology*, Volume 18, Issue 5, Pages 635-655, 2001.



- IPCC-Intergovernmental Panel on Climate Change: IPCC Special Report on Carbon Dioxide Capture and Storage, Prepared by Working Group III of the Intergovernmental Panel on Climate Change [Metz, B., Davidson, O., de Coninck, H. C., Loos, M., and Meyer, L.A. (Eds.)], Cambridge University Press, Cambridge, United Kingdom and New York, NY, USA, 2005.
- Juanatey, M., Tryggvason, A., Juhlin, C., Bergström, U., Hübert, J., and Pedersen, L.B.: MT and reflection seismics in
5 northwestern Skellefte Ore District, Sweden, *Geophysics*, 78(2), B65-B76, doi: 10.1190/geo2012-0169.1, 2013.
- Juhlin, C.: Imaging of fracture zones in the Finnsjön area, central Sweden, using the seismic reflection method, *Geophysics*, 60(1), 66–75, 1995.
- Lawton, D. C.: Computation of refraction static corrections using first-break traveltimes differences, *Geophysics*, 54(10), 1289–1296, 1989.
- 10 MacGregor, L.: Integrating seismic, CSEM, and well log data for reservoir characterization, *The Leading Edge*, 31(3), 268–277, 2012.
- Malehmir, A., and Bellefleur, G.: 3D seismic reflection imaging of volcanic-hosted massive sulfide deposits: Insights from reprocessing Halfmile Lake data, New Brunswick, Canada, *Geophysics*, 74(6), B209, 2009.
- Moorkamp, M., Heincke, B., Jegen, M., Roberts, A. W., and Hobbs, R. W.: A framework for 3-D joint inversion of MT,
15 gravity and seismic refraction data, *Geophysical Journal International*, 184(1), 477–493, doi: 10.1111/j.1365-246X.2010.04856.x, 2011.
- Martínez-Landa, L., Rötting, T. S., Carrera, J., Russian, A., Dentz, M., and Cubillo, B.: Use of hydraulic tests to identify the residual CO₂ saturation at a geological storage site, *International Journal of Greenhouse Gas Control*, 19, 652–664, 2013.
- Muñoz, G., Ritter, O., and Moeck, I.: A target-oriented magnetotelluric inversion approach for characterizing the low
20 enthalpy Gross Schoenebeck geothermal reservoir, *Geophysical Journal International*, 183(3), 1199–1215, 2010.
- Nakatsuka, Y., Xue, Z., Garcia, H., and Matsuoka, T.: Experimental study on CO₂ monitoring and quantification of stored CO₂ in saline formations using resistivity measurements, *International Journal of Greenhouse Gas Control*, 4, 209–216, doi: 10.1016/j.ijggc.2010.01.001, 2010.
- Nisi, B., Vaselli, O., Tassi, F., Elío, J., Delgado Huertas, A., Mazadiego, L.P., and Ortega, M.F.: Hydrogeochemistry of
25 surface and spring waters in the surroundings of the CO₂ injection site at Hontomín-Huermeces (Burgos, Spain), *International Journal of Greenhouse Gas Control*, 14, 151–168, 2013.
- Ogaya, X., Ledo, J., Queralt, P., Marcuello, Á., and Quintà, A.: First geoelectrical image of the subsurface of the Hontomín site (Spain) for CO₂ geological storage: A magnetotelluric 2D characterization, *International Journal of Greenhouse Gas Control*, 13, 168–179, 2013.
- 30 Ogaya, X., Queralt, P., Ledo, J., Marcuello, A., and Jones, A.G.: Geoelectrical baseline model of the subsurface of the Hontomín site (Spain) for CO₂ geological storage in a deep saline aquifer: a 3D Magnetotelluric characterisation, *International Journal of Greenhouse Gas Control*, 27, 120–138, 2014.



- Permanyer, a., Márquez, G., and Gallego, J. R. R.: Compositional variability in oils and formation waters from the Ayoluengo and Hontomín fields (Burgos, Spain). Implications for assessing biodegradation and reservoir compartmentalization, *Organic Geochemistry*, 54, 125–139, 2013.
- Quintà, A., and Tavani, S.: The foreland deformation in the south-western Basque-Cantabrian Belt (Spain). *Tectonophysics*, 576-577, 4–19, 2012.
- Rubio, F.M., Ayala, C., Gumiel, J.C., and Rey, C.: Caracterización mediante campo potencial y teledetección de la estructura geológica seleccionada para planta de desarrollo tecnológico de almacenamiento geológico de CO₂ en Hontomín (Burgos), IGME- Instituto Geológico y Minero de España Technical Report, 182 pp, 2011.
- Solon, F. F., Fontes, S. L., and Meju, M. A.: Magnetotelluric imaging integrated with seismic, gravity, magnetic and well-log data for basement and carbonate reservoir mapping in the São Francisco Basin, Brazil, *Petroleum Geoscience*, 21(4), 285–299, 2015.
- Taner, M. T., Wagner, D. E., Baysal, E., and Lu, L.: A unified method for 2-D and 3-D refraction statics, *Geophysics*, 63(1), 260, 1998.
- Tryggvason, A., Schmelzbach, C., and Juhlin, C.: Traveltime tomographic inversion with simultaneous static corrections — Well worth the effort, *Geophysics*, 74(6), WCB25–WCB33, 2009.
- Ugalde, A., Villaseñor, A., Gaite, B., Casquero, S., Martí, D., Calahorrano, Marzán, I., Carbonell, R., and Estaun, A. P.: Passive Seismic Monitoring of an Experimental CO₂ Geological Storage Site in Hontomín (Northern Spain), *Seismological Research Letters*, 84(1), 75–84, 2013.
- Vilamajó, E., Queralt, P., Ledo, J., and Marcuello, A.: Feasibility of Monitoring the Hontomín (Burgos, Spain) CO₂ Storage Site Using a Deep EM Source, *Surveys in Geophysics*, 34, pp. 441–461, 2013.
- Vilamajó, E., Rondeleux, B., Queralt, P., Marcuello, A., and Ledo, J.: A land controlled-source electromagnetic experiment using a deep vertical electric dipole: experimental settings, processing, and first data interpretation, *Geophysical Prospecting*, 63, 1527-1540, 2015.
- Werthmüller, D., Ziolkowski, A., and Wright, D.: Background resistivity model from seismic velocities, *Geophysics*, 78(4), E213-E223, doi: 10.1190/GEO2012-0445.1, 2013.
- White, D.: Seismic characterization and time-lapse imaging during seven years of CO₂ flood in the Weyburn field, Saskatchewan, Canada. *International Journal of Greenhouse Gas Control*, 16(1), 2013, doi: [10.1016/j.ijggc.2013.02.006](https://doi.org/10.1016/j.ijggc.2013.02.006).
- Woodward, D. J.: Inversion of Seismic Refraction Data, Geophysics Division Technical Report No. 114 (available from GNS, <http://www.gns.cri.nz/>), 1991.



Table 1. Empirical Relation ER1: linear regression of V vs $\log(R)$

Relationship	Depth (m)	a	b	Norm of residuals
S1	0-100	2682.5	-1329.5	25058
S2	100-150	1413.5	490.27	30983
S3	150-200	2393.8	-545.05	27627
S4	200-300	-46.979	2392.9	20606
S5	300-400	46.802	2327.1	10672
D1	456-573	95.35	2801.2	7323.7
D2	573-620	718.6	1884.1	4309.7
D3	620-750	427.99	2282.4	9749.6
D4	750-958	315.28	2702.2	10060
D5	958-986	113.32	3144.6	3281.6
D6	986-1076	56.009	3508.8	10962
D7	1076-1150	1231.1	2562.4	7303.4
D8	1150-1193	1385.5	2550.9	2538.1
D9	1193-1239	1787.6	2090.5	2201.6
D10	1239-1411	1938.7	2102	4060.9
D11	1411-1442	-230.23	4175.1	5340.8
D12	1442-1611	1127.8	3217.1	19653

5

10

15



Table 2. Empirical Relation ER2: linear regression of R/V vs R

Relationship	Depth (m)	c	d	Norm of residuals
S1	0-100	0.00017	0.008	0.16
S2	100-150	0.00036	0.0023	0.2
S3	150-200	0.00024	0.0037	0.11
S4	200-300	0.00043	0.00062	0.17
S5	300-400	0.00041	0.00048	0.12
D1	456-573	0.00033	0.00056	0.14
D2	573-620	0.00025	0.0059	0.09
D3	620-750	0.00029	0.0035	0.27
D4	750-958	0.00028	0.0017	0.21
D5	958-986	0.0003	-0.0009	0.09
D6	986-1076	0.00029	-0.00054	0.07
D7	1076-1150	0.00018	0.0018	0.04
D8	1150-1193	0.00018	0.00096	0.01
D9	1193-1239	0.00017	0.00094	0.004
D10	1239-1411	0.00018	0.00065	0.004
D11	1411-1442	0.00031	-0.00068	0.008
D12	1442-1611	0.00016	0.001	0.08

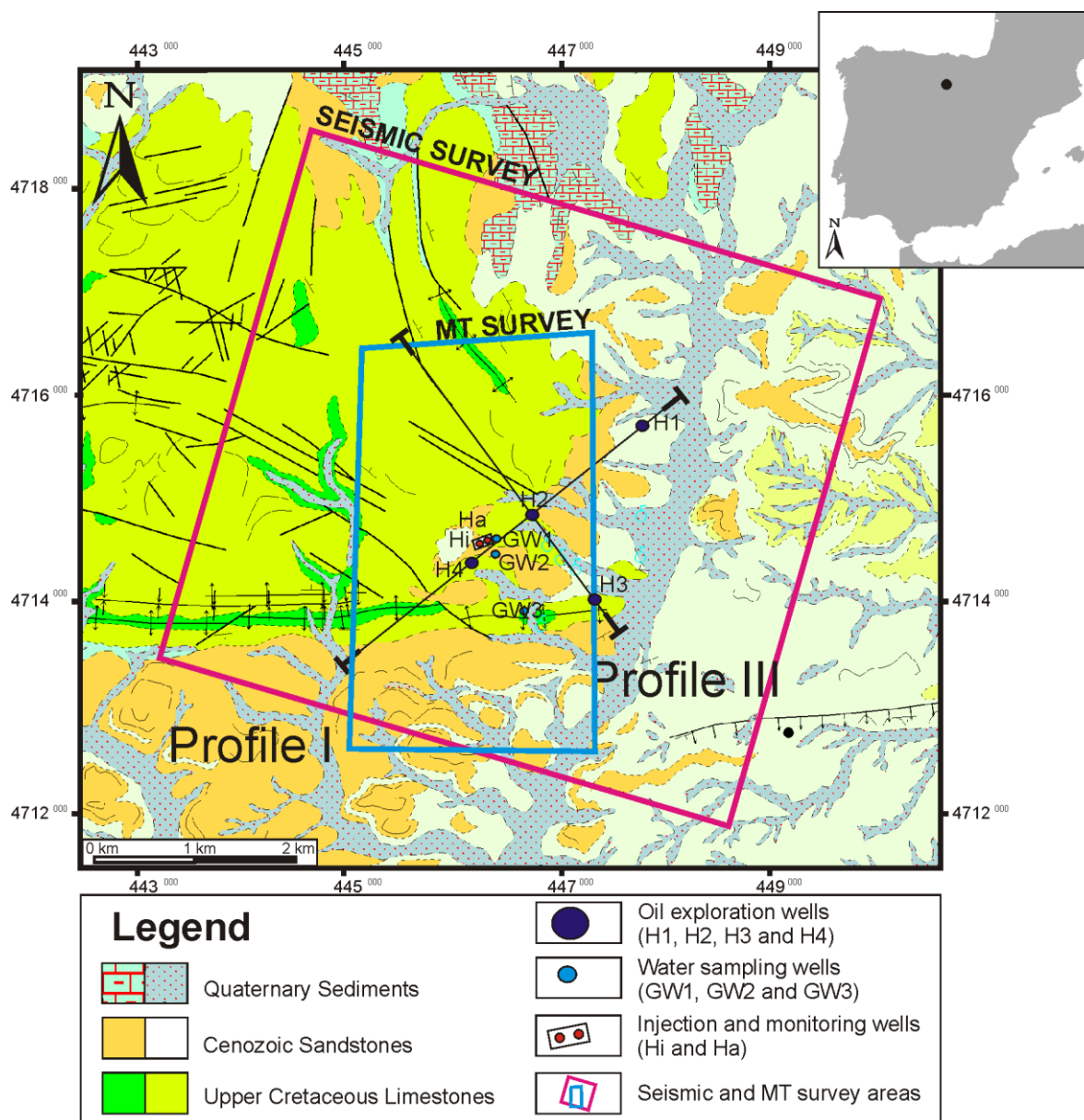


Figure 1. Location of the study area, MT survey, seismic survey and wells. Profiles I and III refer to the position of the cross-sections shown in Fig. 5.

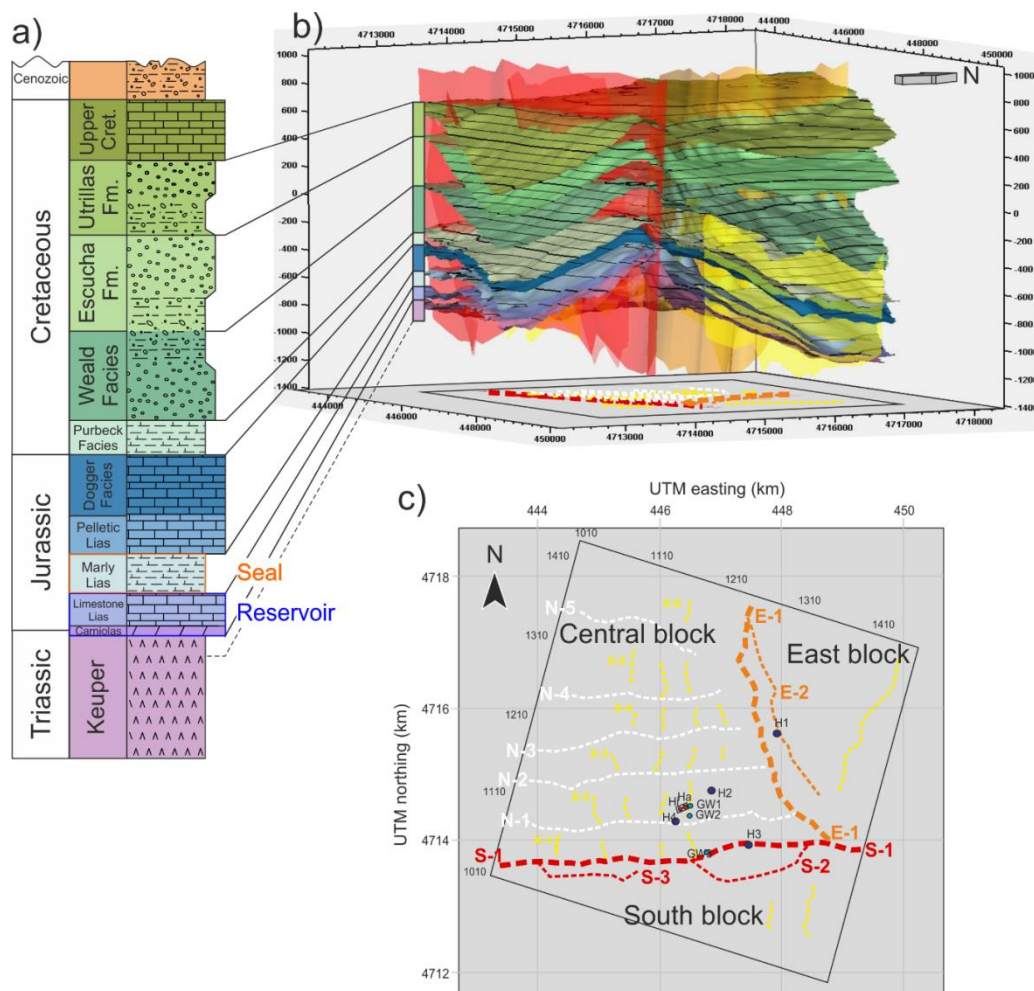


Figure 2. Description of the lithologies and structures interpreted in the subsurface of Hontomín (after Alcalde et al., 2014).

(a) Stratigraphic column with relative thicknesses of the sediments. (b) 8-layered structural model interpreted from the seismic and well-log data; the eight surfaces interpreted are: Anhydrite Unit (top Keuper), Limestone Lias (top of the reservoir formation), Marly Lias (top of the primary seal formation), Dogger facies, Purbeck facies, Weald facies, Escucha fm. and Utrillas fm. (c) Sketch with the general distribution and labeling of the main faults interpreted in the study area, including: “S-faults” in red, “E-faults” in orange, “N-faults” in white and “X-faults” in yellow; S-1 corresponds to the South fault and E-1 corresponds to the East fault; these two faults determine the remarkable division of the study area in three blocks: the East, the Central and the South block. The position of the oil exploration and water wells are also included for reference.

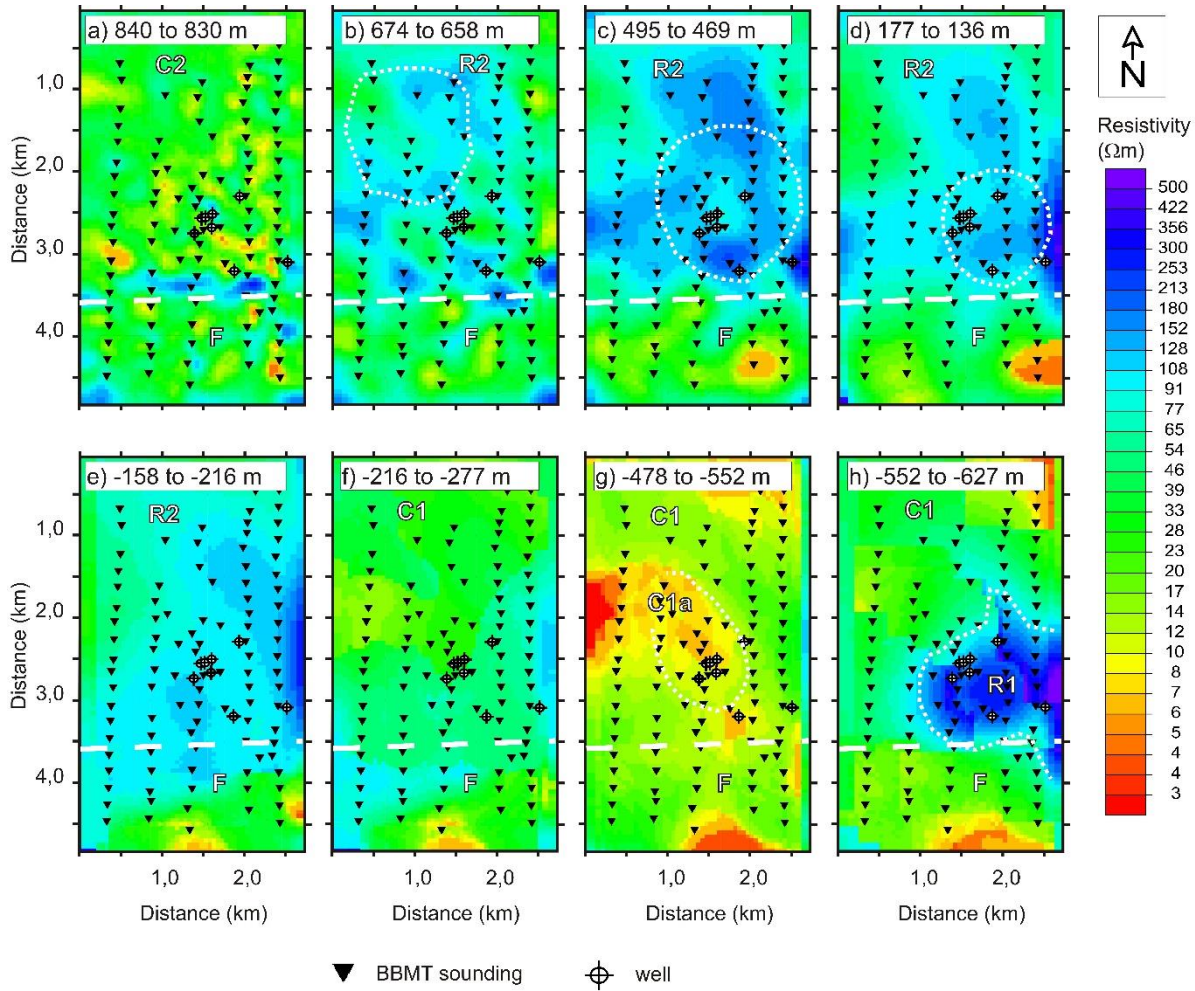


Figure 3. 3D geoelectrical model (reproduced from Ogaya et al., 2014). Z-slices of the model from top (a) to bottom (h), depths are indicated in each sub-plot. The main resistivity layers (R1, C1, R2 and C2) and the F region are marked. EW white dashed line indicates the approximate north-border of the F region. From bottom to top (depths given in terms of m.a.s.l.): h) top of the R1 layer; g) main reservoir C1a (saline aquifer); f) top of the C1 layer; e) bottom of the R2 layer; d), c) and b) evolution of the R2 layer's dome structure and a) C2 layer and bend of the R2 layer due to the presence of the F region. (See Ogaya et al., 2014 for more information.)

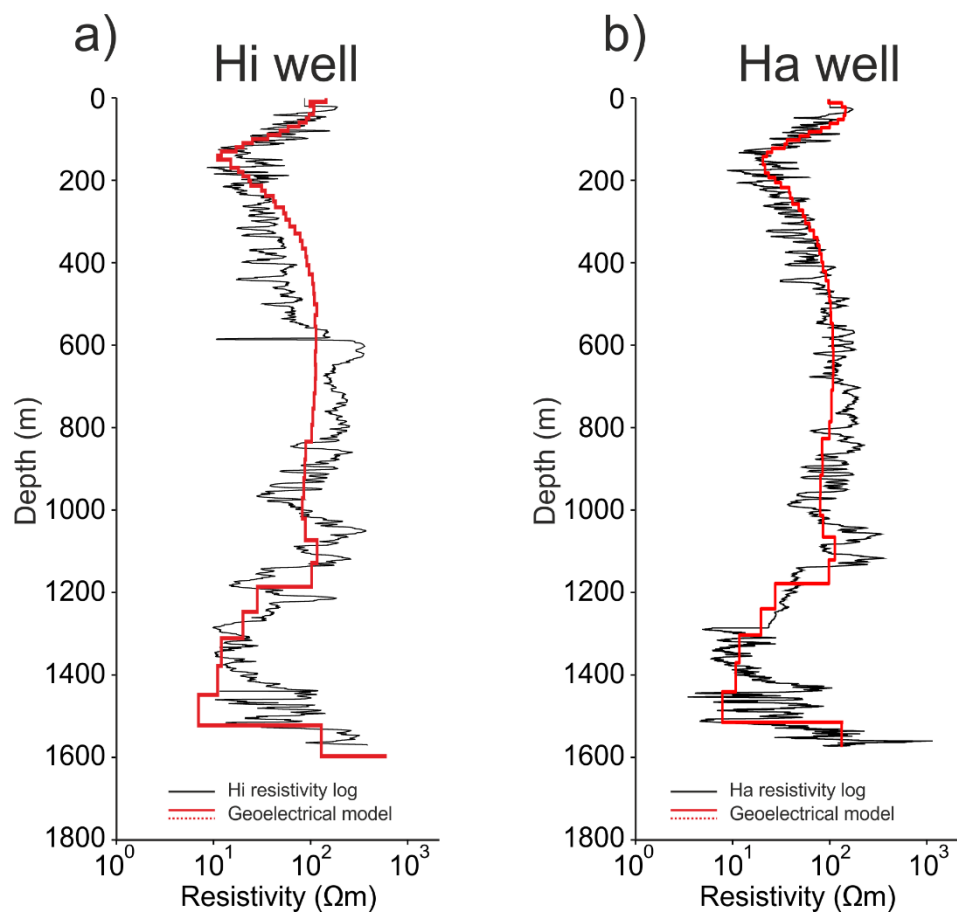


Figure 4. Comparison between the resistivity log data (in black) and 1D model provided by the column of the 3D resistivity model located at the well position (in red) for the Hi (a) and Ha (b) wells.

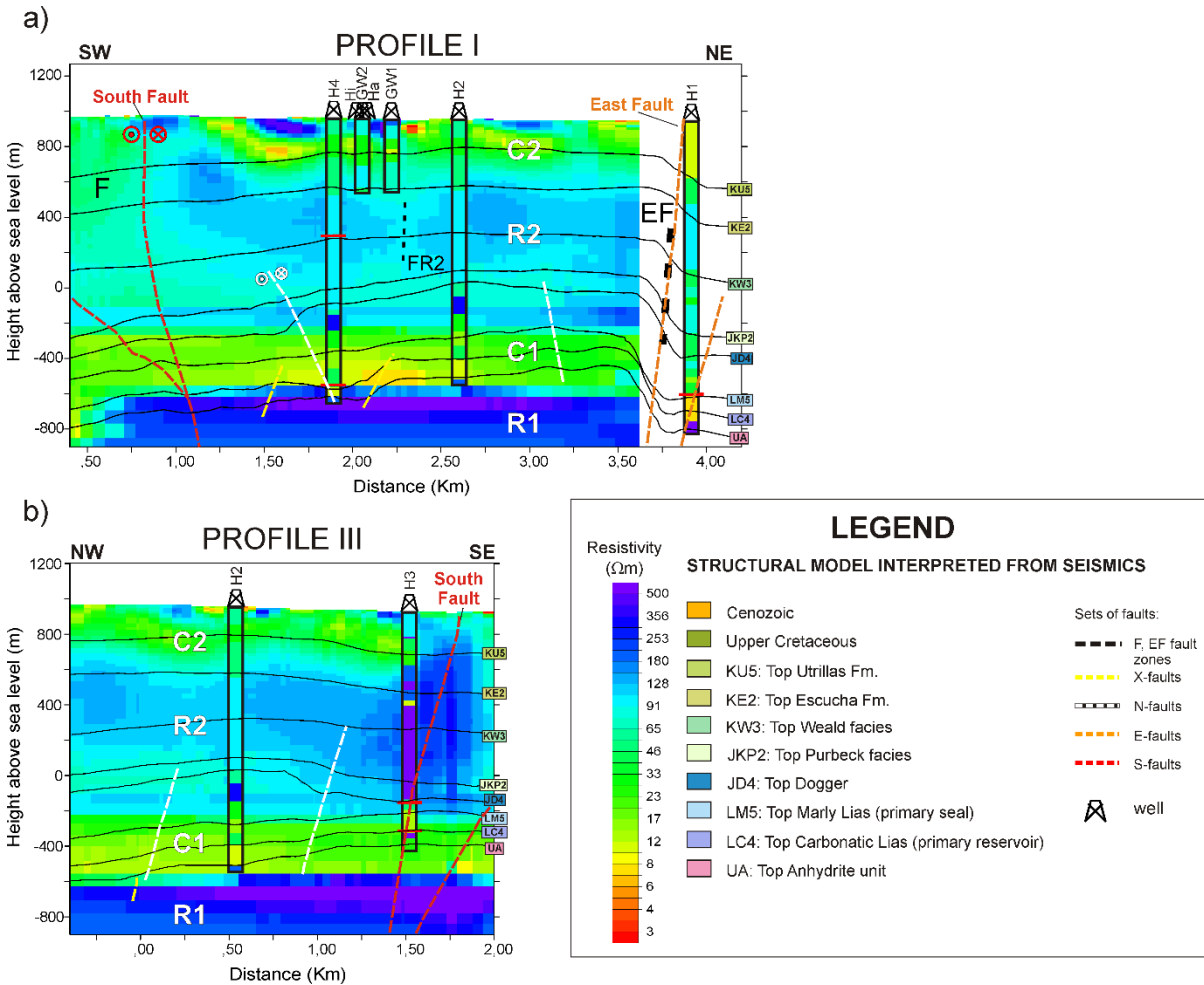


Figure 5. Joint structural interpretation. (a) Profile I of the 3D MT model and superimposed, α profile of the 3D seismic model. (b) Section III of the MT model and superimposed, β profile of the seismic model. Geoelectrical model: the main resistive layers (R1, C1, R2 and C2) and the F and EF fault regions are indicated. Possible FR2 fracture regions are also specified. The 1D resistivity models derived in Ogaya et al. (2014) for each well appear superimposed. Seismic model: the top of the main units (black lines) and the main fault sets (X-fault, N-faults, E-faults and S-faults) are indicated.

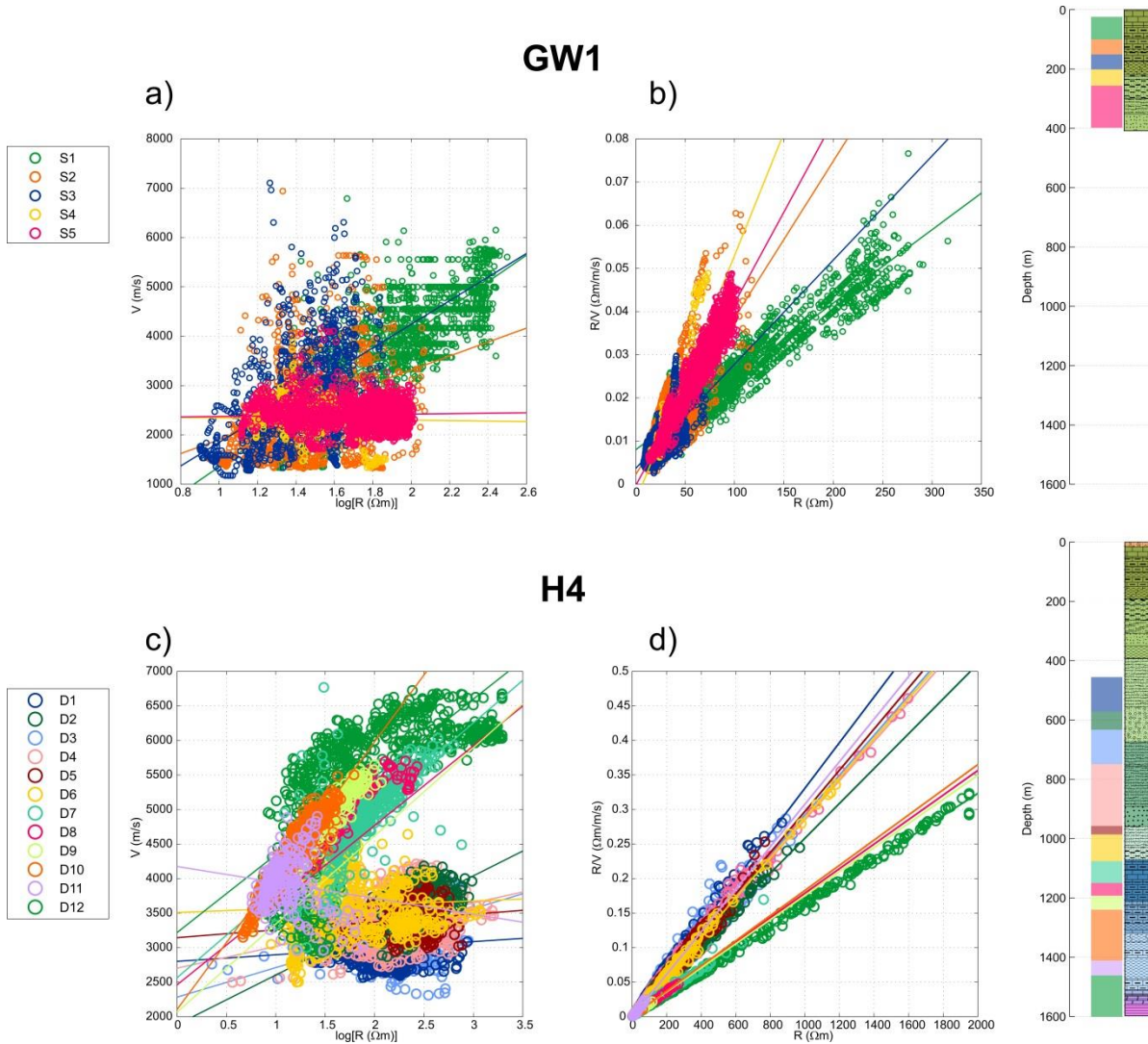


Figure 6. Resistivity vs Velocity for the GW1 and the H4. The resistivity-velocity log pairs were grouped based on their depth and their relative behaviour: the GW1 log data were divided into five groups (S-groups) and the H4 log data into twelve groups (D-groups). Two empirical relations were calculated for each group: (i) ER1, a linear regression of V vs $\log(R)$ (b and c) and (ii) ER2, a linear regression of R/V vs R (b and d).

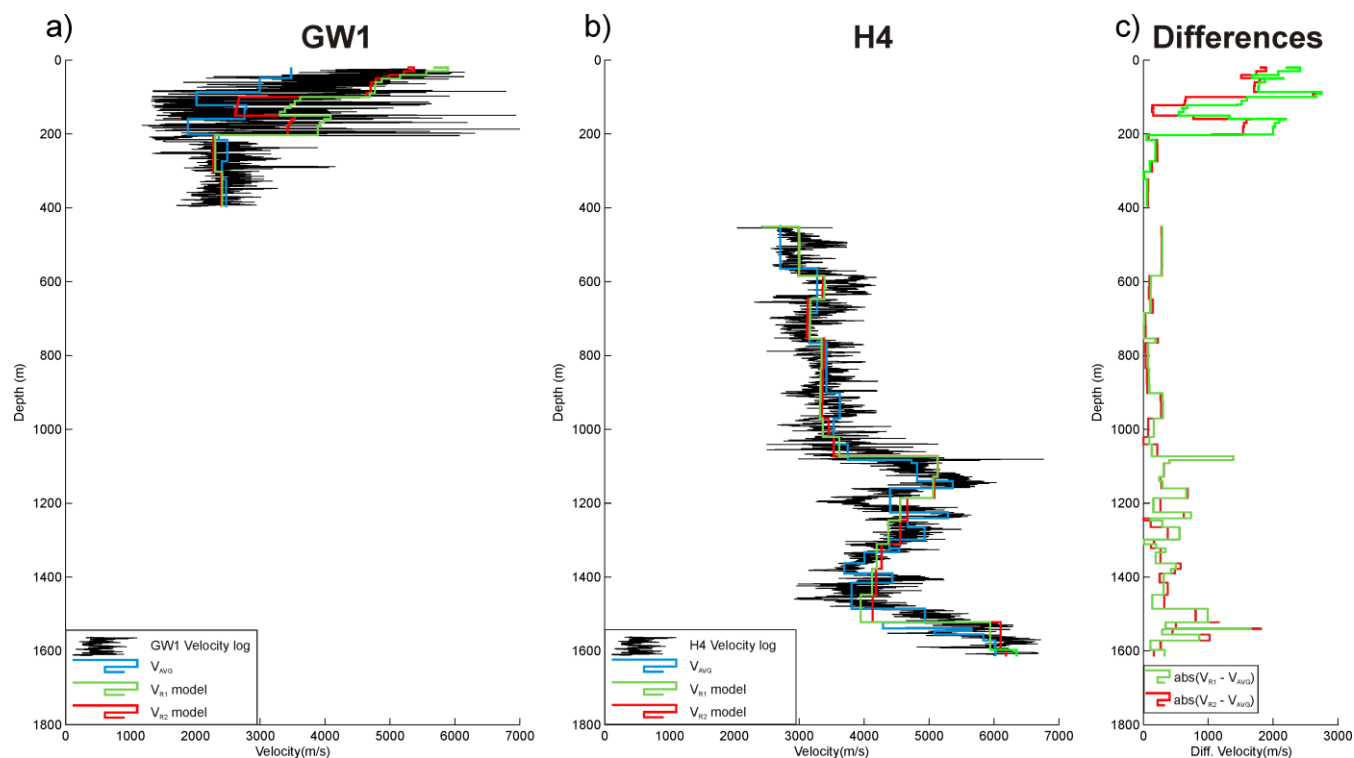


Figure 7. Velocity log data (in black), 1D velocity models provided by V_{R1} (in green), V_{R2} (in red) and V_{AVG} (in blue) for the GW1 (a) and the H4 (b) wells and differences between the V_R models and V_{AVG} (c).

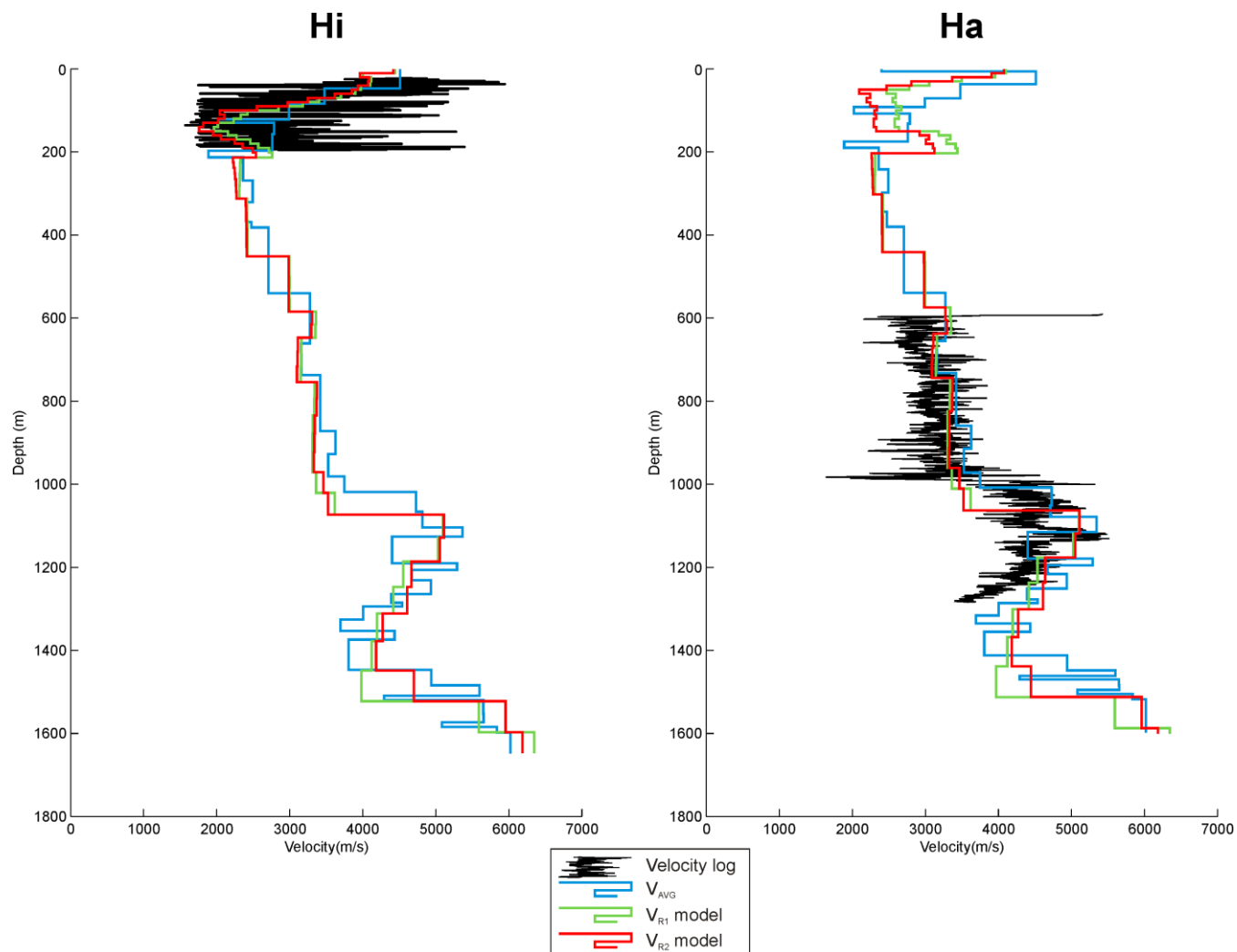


Figure 8. Velocity log data (in black) and 1D velocity wells provided by the VR1 (in green) and VR2 (in red) models for the Hi and the Ha wells together with the prognosis of this two wells published in Alcalde et al. (2014, V_{AVG} models, in blue).

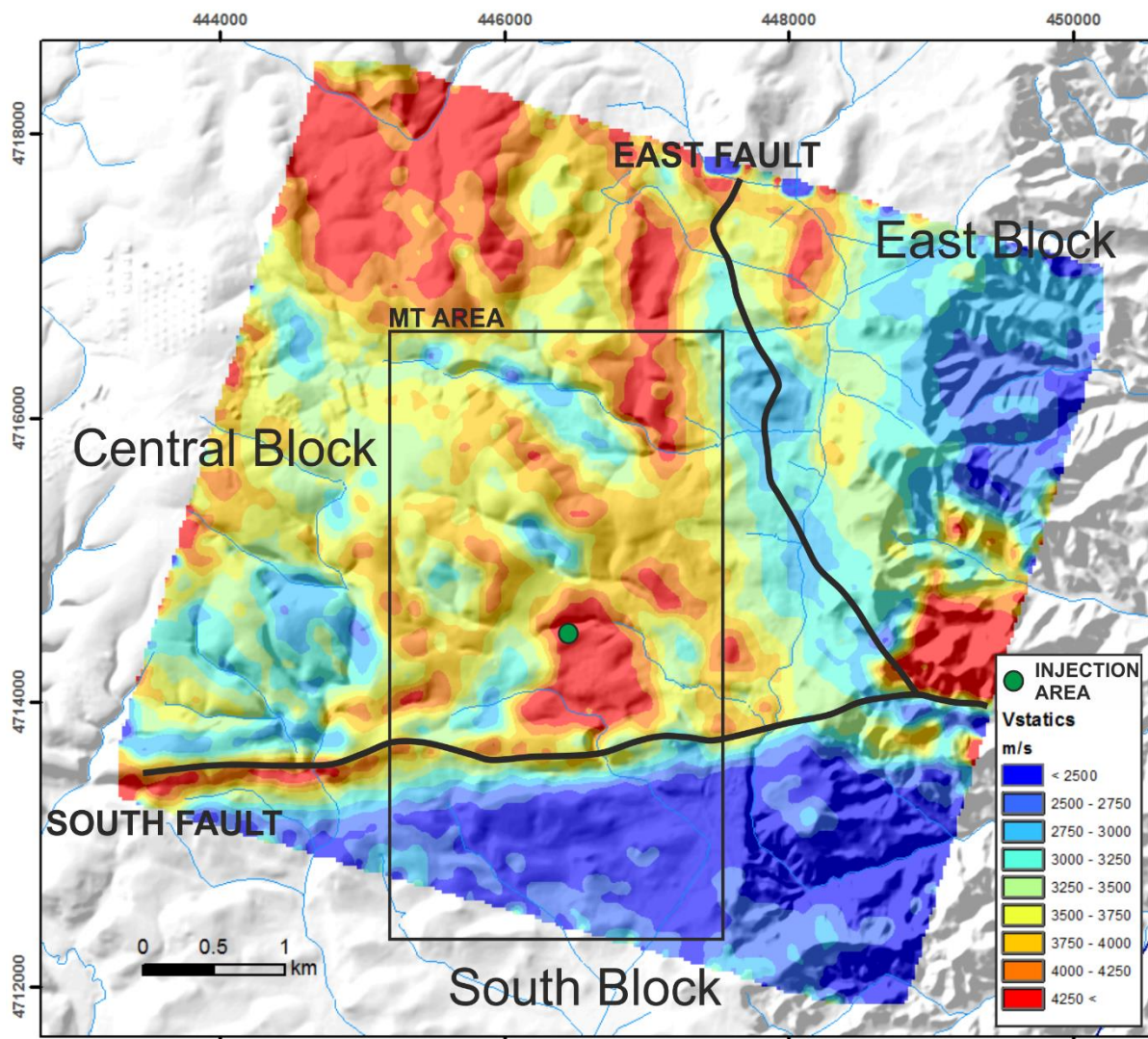


Figure 9. Velocity model used in the static correction calculations, with the area covered by the MT. The position of the East and South faults, extracted from the seismic data, divides the study area in the Central, East and South blocks. Note that the two faults do not outcrop in the study area.

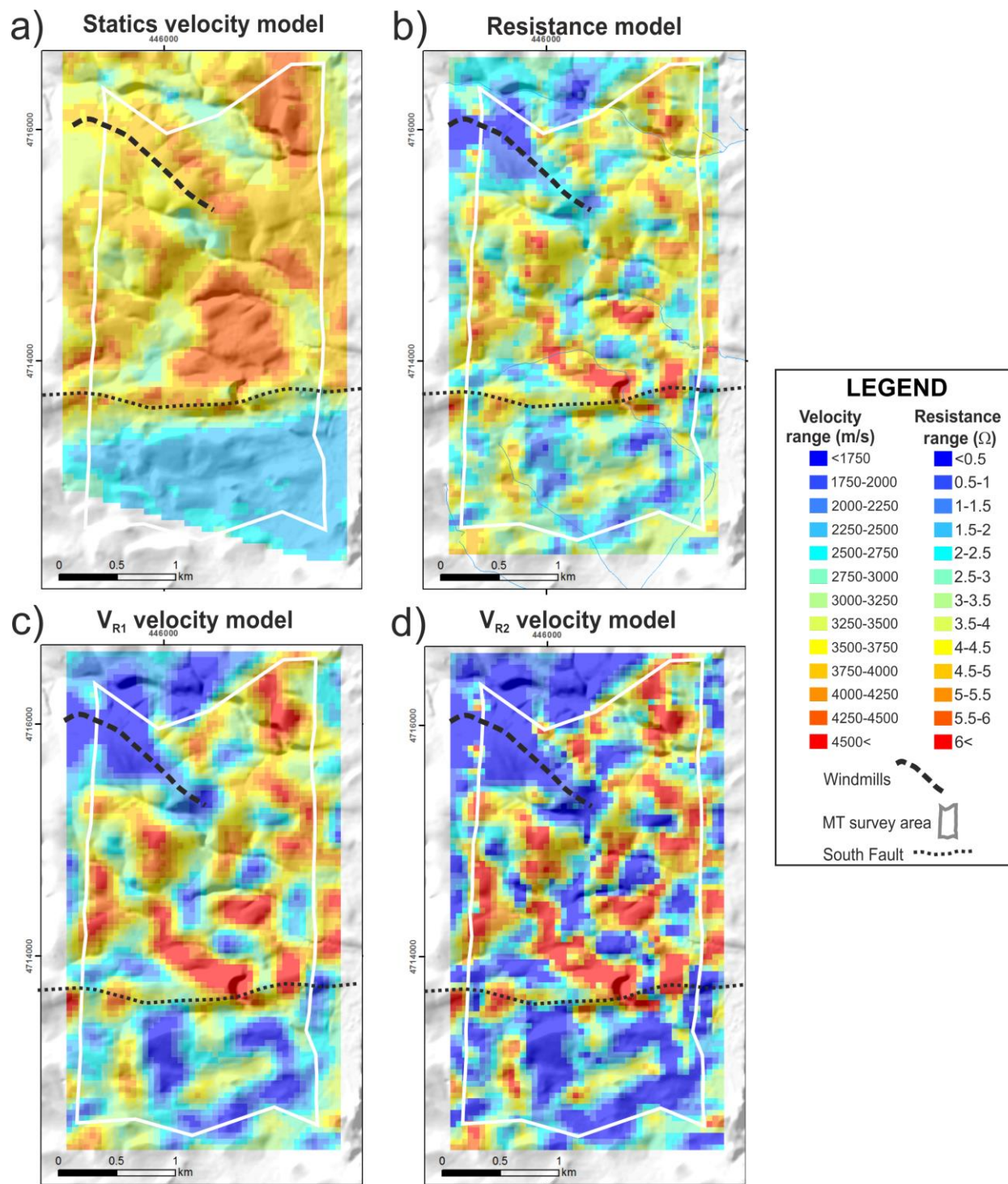


Figure 10. Static correction model from seismic (a), resistance model for the first 40 m (b) and replacement velocity model for the first 40 m computed using V_{R1} (c) and V_{R2} (d).